Composites Part C: Open Access 18 (2025) 100636

Contents lists available at ScienceDirect

Composites Part C: Open Access

journal homepage: www.sciencedirect.com/journal/composites-part-c-open-access

Fibre-orientation-driven defect probability mapping for machining-induced delamination and burr minimisation in carbon fibre-reinforced polymer (CFRP) composites

Norbert Geier

Department of Manufacturing Science and Engineering, Faculty of Mechanical Engineering, Budapest University of Technology and Economics, Műegyetem rkp. 3., H-1111 Budapest, Hungary

ARTICLE INFO

Keywords:
Milling
Composite
CFRP
Delamination
Burr
Optimisation

ABSTRACT

Machining-induced burrs and delamination compromise the integrity of polymer composite components reinforced by chopped carbon tows. An image-based optimisation algorithm was therefore developed that locates the ideal hole centre within the preform allowance to minimise defect risk. High-resolution images, captured under multiple lighting conditions, are processed to generate a probability map of burr and delamination formation. Then, recursive convolution yielded a matrix whose minima identified the optimal hole position. First, edge trimming experiments were conducted to determine the arguments (critical fibre cutting angle and its range) of the developed algorithm. Up-milling was confirmed to outperform down-milling, yielding an order-of-magnitude smaller burr heights and a narrower defect-critical fibre cutting angle range. Then, based on the edge trimming results, holes were circular-milled, and demonstrated that the optimised "best-case" centre reduced average contour height by 64.99 % and contour-depth by 86.51 %, while burr- and delamination-area metrics improved by 84.90 % and 77.07 %, respectively, underlying the efficiency and importance of the proposed method. Implemented at TRL 4 with standard CNC equipment and open-source Python scripts, the method offers a practical framework for integrating burr- and delamination minimisation into CFRP component design and manufacturing process planning.

1. Introduction

Carbon fibre-reinforced polymer (CFRP) composites have become indispensable in aerospace, automotive and renewable-energy applications due to their exceptional strength-to-weight ratios and formability [1]. Despite advances in lay-up, curing and preforming technologies, mechanical machining —particularly drilling [2] and milling [3]— remains essential for achieving the precise geometries and tight tolerances demanded by modern designs. Over the past decade, researchers and tool manufacturers have introduced a variety of high-performance solutions to minimise machining-induced delamination, burr formation and surface damage during the production of holes in CFRP laminates.

Although the use of diamond-coated, W-shaped solid-carbide drills [4–7], coupled with optimised process parameters [8] and entry/exit feed-rate control [9], has proven capable of producing hundreds of CFRP holes with negligible delamination and burrs under cryogenic conditions [10]. However, cryogenic cooling entails a substantial carbon footprint and operational cost; diamond coatings and precision feed-control units are expensive, and the complex grinding required to manufacture W-shaped tools further elevates tooling costs. Alternative approaches such as helical milling [11], tilted helical milling [12] and wobble milling [13] offer effective control of cutting forces —thereby reducing interlaminar damage— but require multi-axis interpolations that are challenging to program and integrate into high-volume manufacturing lines. Ultrasonic vibration–assisted machining has been shown to reduce cutting forces by up to 30 % [14], slow tool wear rates and produce holes with markedly lower burr height and delamination compared with conventional drilling [15–17]. However, retrofitting high-frequency actuators into standard CNC drilling spindles presents significant engineering challenges, such as maintaining vibration amplitude under load and ensuring reliable tool-holder coupling, which have limited widespread adoption in production environments.

Other innovative strategies have targeted the unique difficulties posed by fibrous composites. For example, pilot-hole techniques (pre-drilling a small-diameter guide hole) can reduce thrust force and improve hole circularity [18,19]; support plates placed beneath the

E-mail address: geier.norbert@gpk.bme.hu.

https://doi.org/10.1016/j.jcomc.2025.100636

Available online 12 August 2025

workpiece almost eliminate exit-side delamination [20,21]; and laser-assisted machining softens the polymer matrix ahead of the cutting edge, enabling cleaner fibre separation at the expense of higher capital cost and the need for precise beam alignment [22,23]. While each of these methods offers distinct sustainability or quality advantages, they often require specialised equipment or process steps that complicate integration into high-volume aerospace and automotive production lines.

Although these innovations have extended the practical limits of CFRP hole quality, they largely overlook a key material attribute: fibre orientation. It is well known that the angle between the local fibre direction and the cutting speed vector (the “fibre cutting angle”) governs chip-formation mechanics [24–26], cutting forces [27,28], temperature distributions [29], surface roughness [30] and the initiation of delamination and burrs [31,32]. Consequently, more and more work has incorporated fibre orientation into predictive models and process guidelines. For example, Wang et al. [33] investigated milling forces, surface roughness and tool wear at fibre orientations of 0°, 30°, 45°, 60° and 90°, demonstrating that 45° yields optimal surface finish under their conditions; Geier [28] analysed up and down milling of CFRPs and observed that intermediate fibre orientation angles (≈ 45°-60°) often results in lower instantaneous cutting forces because chip formation shifts from pure bending to a combination of shear and compression; Wang et al. [34] quantified how different fibre cutting angles affect tool flank wear, cutting forces, burr area and surface roughness, while observing that 45° tends to minimise burr formation; Qian et al. [35] simulated temperature and stress fields in unidirectional CFRP turning and reported that maximum tool-edge temperature and stress occurred at 90° of fibre cutting angle, since shearing across fibres produces concentrated heat; and more recently, Geier et al. [36] demonstrated automated detection of fibre tows (i.e., fibre directions) via digital image processing and machine learning, enabling the prediction of hole quality [37].

Despite these advances, existing hole-machining technologies do not exploit fibre orientation maps when planning machining technology. This omission represents a significant research gap: a hole position that avoids critical fibre cutting angles could inherently reduce defect probability without additional tooling complexity. Accordingly, the principal objective of the present study is to develop and experimentally validate a hole-positioning methodology that integrates local fibre direction information into the machining allowance and tool path planning, thereby minimising machining-induced delamination and burr formation in plate-like CFRP composites.

2. Optimisation algorithm exploiting fibre orientation

2.1. Interpretation and goals

The positions of holes in plate-like CFRP composite components can typically only be varied within a very narrow range ($\ll \varnothing 1$ mm), constrained by the positional tolerance specified by the designer. However, due to the inherent inaccuracies of manufacturing equipment and associated technologies, it is advisable to place the centre of the machined hole at the geometric centre of the tolerance zone. For this reason, it is not recommended to alter the geometric relationships between individual holes and either the component’s external contour or other elements of the hole pattern.

Nevertheless, if both the external contour and internal geometric features (e.g., holes, pockets, slots, etc.) of the plate-like CFRP composite part are to be produced by mechanical machining, i.e., by chip removal (as shown in Fig. 1), then by adjusting the lateral external machining allowance of the CFRP preform ($R > 1$ mm), the positions of the machined geometric features —interpreted within the preform— can be optimised to minimise the probability of machining-induced burr and delamination formation.

The magnitude of the lateral external machining allowance (R) in classical preform design is typically determined based on the maturity and accuracy of the preforming technology (e.g., lamination, vacuum infusion), the specified tolerances, as well as the machining process and the cutting tool employed. For plate-like components, this generally results in a uniform allowance around the outer contour (see Fig. 1b). However, Fig. 1c illustrates an allowance strategy in which the lateral external allowance is non-uniform —an approach that may appear unconventional when viewed through the lens of traditional machining allowance practices. It is worth investigating whether, beyond conventional design considerations, it is relevant to account for the influence of machining allowance on the contour-adjacent formation of machining-induced burrs and delamination. Specifically, it asks whether an

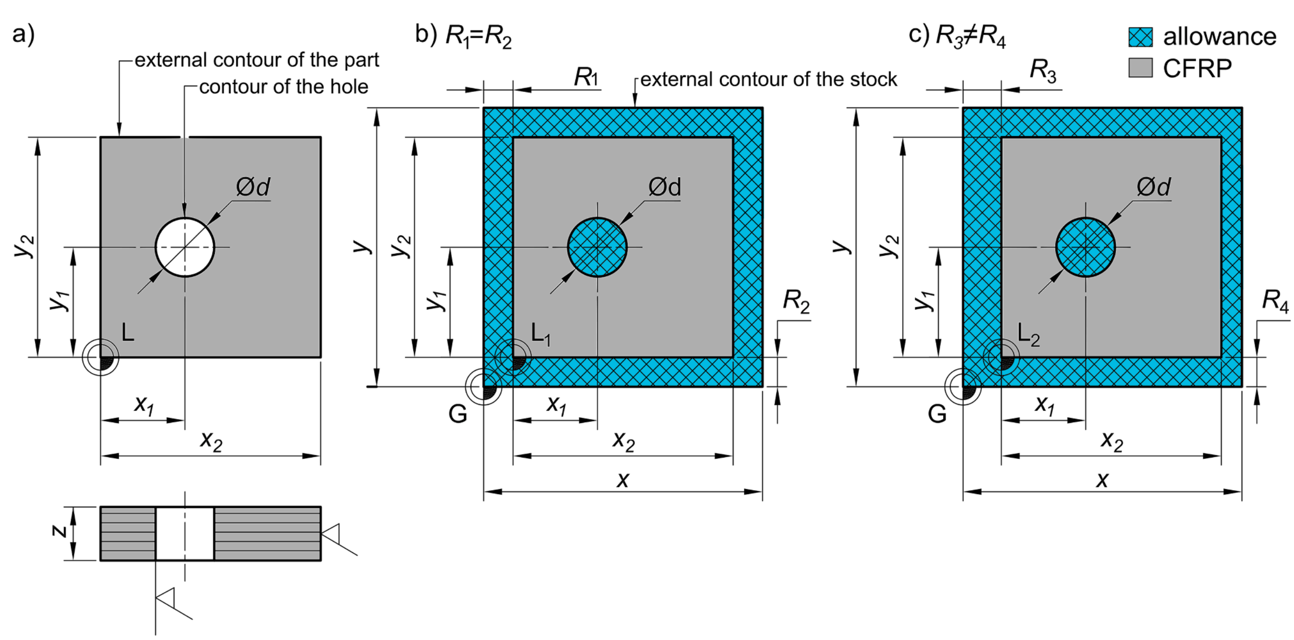

Fig. 1. A schematic illustration of machining allowance strategies for a plate-like CFRP composite component: a) plate-like CFRP sample component; b) conventional preform allowance strategy ($R_1 = R_2$); c) advanced preform allowance strategy ($R_3 \neq R_4$), where L and G denote the datum point of the component and the preform, respectively (redrawn based on Ref [38]).

industrially applicable edge-contour positioning optimisation method exists that can minimise the probability of burr and delamination formation along the machined edges of plate-like composite parts.

Fig. 2 illustrates two types of machining allowance strategies. In both cases, the size of the composite preform ($x \times y$), as well as the nominal geometry of the machined component (with an outer bounding size of $x_2 \times y_2$ and a through-hole of diameter $\varnothing d$ centred at position of C (x_1; y_1)), remains the same. Due to the differing geometries of the machining allowances; however, the expected risk of burr and delamination formation along the machined hole contour differs significantly. This is evidenced by the variation in fibre cutting angle (θ) diagrams shown in Fig. 2: assuming a critical fibre-cutting angle of $\theta_c = 135°$, the allowance design on the right offers a more favourable outcome.

2.2. Algorithm

Due to the industrial need for holes and circular pockets, and the constraints imposed by the available technologies, materials, and cutting tools, the investigation of the relevance of component contour position optimisation, interpreted within the preform, was conducted using a hole-type geometric feature. Considering that the proposed algorithm focuses specifically on the avoidance of defect formation resulting from the inappropriate fibre cutting angle and does not consider defects resulting from the peel-up and push-down effects of drilling, milling technology is selected for hole-machining technology. The main steps of the optimisation algorithm are as follows.

(i) Acquire M sets of digital images from the surface of the composite specimen under varying illumination conditions, following the methodology outlined in [37] (See Fig. 3a).

(ii) Convert the acquired images to greyscale, perform segmentation using Otsu's thresholding method, and apply noise reduction in accordance with the digital image processing procedure described in [36]. The resulting data from these processing steps are stored in the matrix $\boldsymbol{P}_q$, as defined by Eq. (1) and illustrated in Fig. 3b, where i and j correspond to the matrix row and column indices, respectively, and q indicates the specific lighting configuration employed.

$$\boldsymbol{P}_q = \begin{pmatrix} p_{11} & \cdots & p_{1m} \\ \vdots & \ddots & \vdots \\ p_{n1} & \cdots & p_{nm} \end{pmatrix}_q, \; i = 1\ldots n; j = 1\ldots m, \; q = 1\ldots M, \; p_{ijq} \in \{0;1\} \tag{1}$$

(iii) Determination of the $\boldsymbol{S}_q$ submatrix from the $\boldsymbol{P}_q$ matrix in accordance with Eq. (2). The optimal hole position will subsequently be sought within the region defined by this $\boldsymbol{S}_q$ matrix. The corner points of the submatrix are defined by the parameters x and y, as illustrated in Fig. 3c.

$$\boldsymbol{S}_q = \begin{pmatrix} s_{11} & \cdots & s_{1m} \\ \vdots & \ddots & \vdots \\ s_{n1} & \cdots & s_{nm} \end{pmatrix}_q, \; s_{11} = p_{y_1 x_1} \text{ and } s_{nm} = p_{y_2 x_2} \tag{2}$$

$$i = 1\ldots n; j = 1\ldots m, \; q = 1\ldots M, \; s_{ijq} \in \{0;1\}$$

(iv) Determination of matrix $\boldsymbol{F}$, which contains the segmented hole contour, in accordance with Eq. (3), where *C(u;v)* is the centre of the nominal hole contour, and r denotes the hole radius – Fig. 3d.

$$\boldsymbol{F} = \begin{pmatrix} f_{11} & \cdots & f_{1m} \\ \vdots & \ddots & \vdots \\ f_{n1} & \cdots & f_{nm} \end{pmatrix} = \begin{cases} 1, & (j-u)^2 + (i-v)^2 = r^2 \\ 0, & \text{else} \end{cases} \tag{3}$$

$$i = 1\ldots n; j = 1\ldots m, f_{ij} \in \{0;1\}$$

(v) Determination of the $\boldsymbol{VC}$ matrix, which defines the distribution of the cutting speed (v_c) vector direction along the hole contour, in accordance with Eq. (4), where $\boldsymbol{E}$ is a 3×3 all-ones matrix – Fig. 3e.

$$\boldsymbol{VC} = \begin{pmatrix} vc_{11} & \cdots & vc_{1m} \\ \vdots & \ddots & \vdots \\ vc_{n1} & \cdots & vc_{nm} \end{pmatrix} = \boldsymbol{F} \cdot \alpha(x, y, u, v) \cdot \boldsymbol{E}, \text{ where}$$

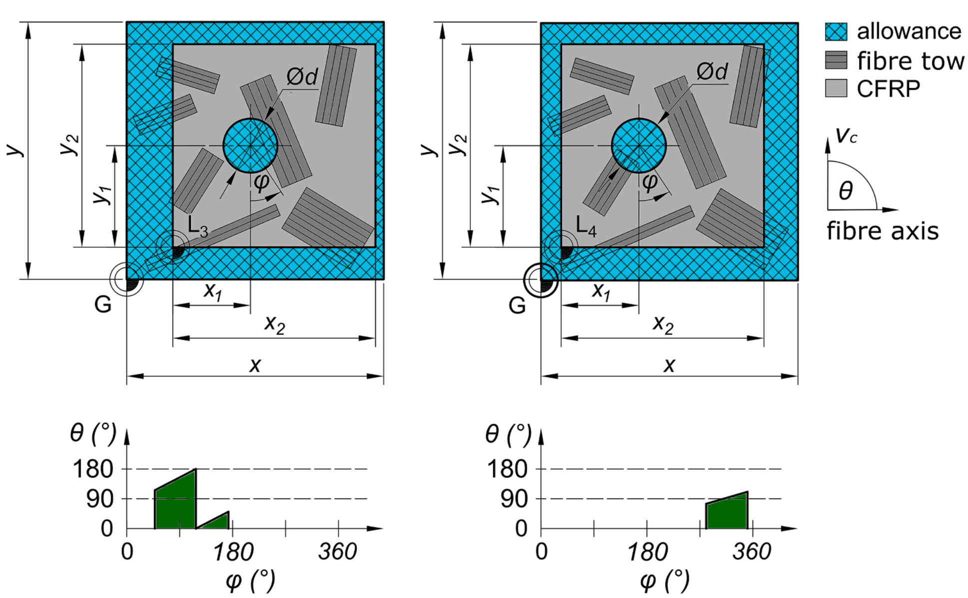

Fig. 2. A schematic illustration of the effect of the machining allowance strategy on the fibre cutting angle (θ) along the hole contour (and thus on the expected machining-induced burr and delamination formation) in a polymer composite reinforced with stochastically positioned and oriented carbon-fibre tows, where φ denotes a running parameter and v_c is the cutting speed (redrawn based on Ref [38]).

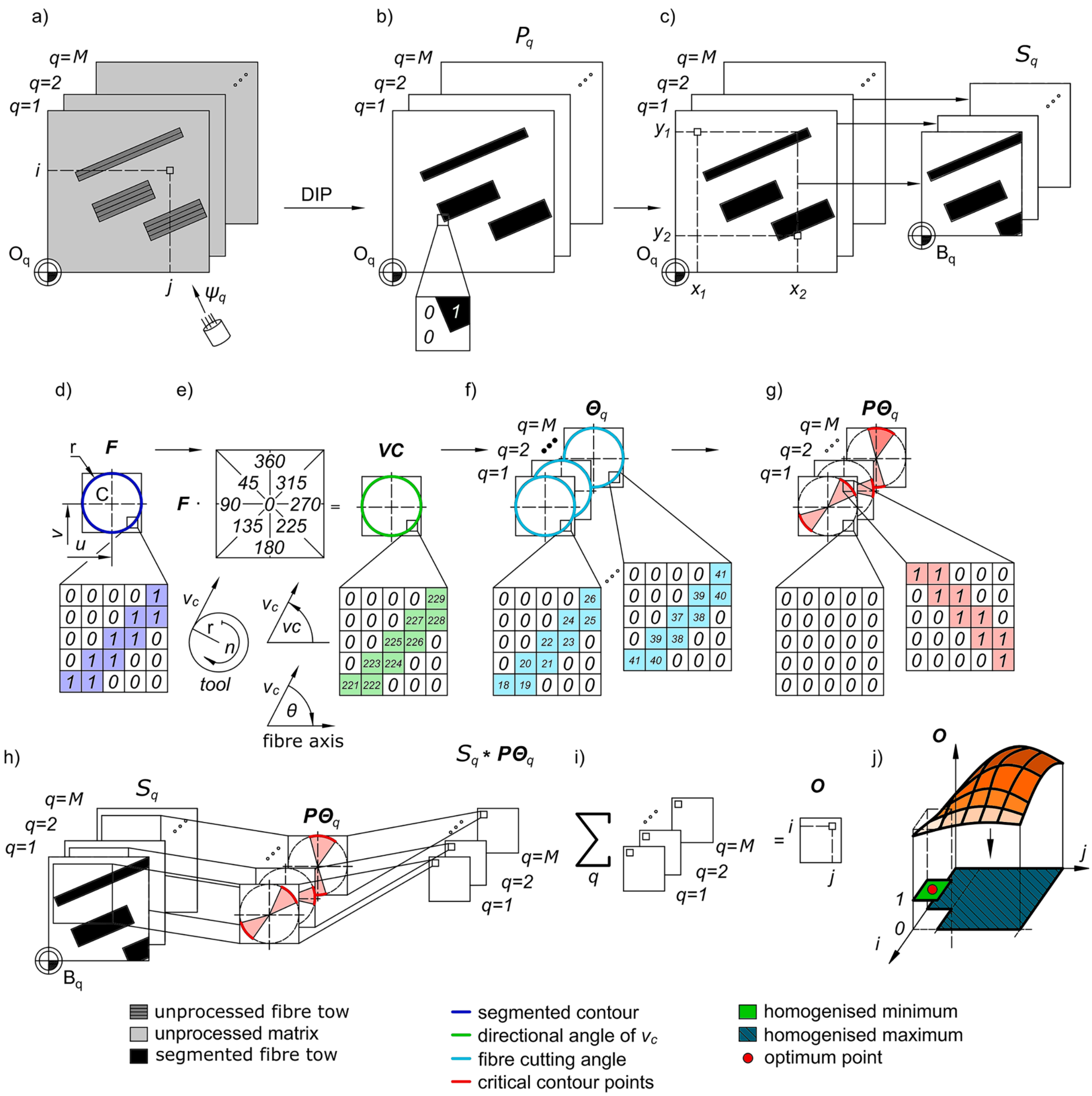

Fig. 3. A schematic illustration of the optimisation algorithm: a) original images; b) digitally processed images; c) formulation of the optimisation domain; d) segmented hole contour; e) cutting speed (v_c) direction angles along the hole contour; f) fibre cutting angle (θ) values along the hole contour; g) probability matrix; h) convolution of the $\boldsymbol{S}$ matrix with the $\boldsymbol{P\theta}$ kernel; i) summation of the convolved matrices; j) normalisation (homogenisation) and optimum point.

$$\alpha(x,y,u,v) = \begin{cases} arctg\left(\frac{|y-v|}{|x-u|}\right) - 90^\circ,\ x > u \text{ and } y > v \\ 90^\circ - arctg\left(\frac{|y-v|}{|x-u|}\right),\ x \le u \text{ and } y > v \\ arctg\left(\frac{|y-v|}{|x-u|}\right) + 90^\circ,\ x \le u \text{ and } y \le v \\ 270^\circ - arctg\left(\frac{|y-v|}{|x-u|}\right), \text{else} \end{cases}$$

$$i = 1\ldots n; j = 1\ldots m, vc_{ij} \in \{0\ldots360\} \tag{4}$$

(vi) Formation of q number of $\boldsymbol{\Theta}$ matrices in accordance with Eq. (5), where each matrix defines the fibre cutting angle (θ) values along the hole contour (see Fig. 3f), where ϕ denotes the fibre orientation angle, i.e., the angle of the fibres relative to the horizontal axis – calculated using the direction of illumination ψ_q (Fig. 3a).

$$\boldsymbol{\Theta}_q = \begin{pmatrix} \theta_{11} & \cdots & \theta_{1m} \\ \vdots & \ddots & \vdots \\ \theta_{n1} & \cdots & \theta_{nm} \end{pmatrix}_q, \text{ where}$$

$$\boldsymbol{\theta} = \begin{cases} vc_{ij} - \phi_q,\ vc_{ij} > \phi_q \text{ and } vc_{ij} \le 180 \\ 180 - (vc_{ij} - \phi_q), vc_{ij} < \phi_q \text{ and } vc_{ij} \le 180 \\ vc_{ij} - \phi_q - 180, \text{ else} \end{cases}$$

$$i = 1\ldots n; j = 1\ldots m,\ q = 1\ldots M,\ \theta_{ijq} \in \{0\ldots180\}, \phi_q \in \{0\ldots180\} \tag{5}$$

(vii) Determination of the probability matrix $\boldsymbol{P\Theta}_q$ based on Eq. (6), where θ_c denotes the critical fibre cutting angle, and δ is the extension of the critical fibre cutting angle region – see Fig. 3g.

$$\boldsymbol{P\Theta}_q = \begin{pmatrix} p\theta_{11} & \cdots & p\theta_{1m} \\ \vdots & \ddots & \vdots \\ p\theta_{n1} & \cdots & p\theta_{nm} \end{pmatrix}_q, \text{ where}$$

$$p\theta_{ijq} = \begin{cases} 1, (\theta_c - \delta_1) < \theta_{ijq} < (\theta_c + \delta_2) \\ 0, \ else \end{cases}$$

$$i = 1...n; j = 1...m, \ q = 1...M, \ p\theta_{ijq} \in \{0...1\} \tag{6}$$

(viii) Convolution of q $\boldsymbol{S}$ matrices using $\boldsymbol{P\Theta}$ kernels, followed by their summation in accordance with Eq. (7) – see Fig. 3h. The elements o_{ij} of matrix $\boldsymbol{O}$ indicate, for each position, the number of critical contour points associated with a high likelihood of defect (burr or delamination) formation, under the assumption of clockwise tool rotation.

$$\boldsymbol{O} = \sum_{q=1}^{M} (\boldsymbol{S} * \boldsymbol{P\Theta})_q = \begin{pmatrix} o_{11} & \cdots & o_{1m} \\ \vdots & \ddots & \vdots \\ o_{n1} & \cdots & o_{nm} \end{pmatrix}$$

$$i = 1...n; j = 1...m, \ q = 1...M, \ o_{ij} \in \{0...M \cdot 2 \cdot r \cdot \pi\} \tag{7}$$

(ix) The normalisation of matrix $\boldsymbol{O}$ according to Eq. (8), using a safety factor ϑ=0.1 and the maximum element (MAX) of $\boldsymbol{O}$.

$$o_{ij} = \begin{cases} 1, \ o_{ij} < (\vartheta \cdot \text{MAX}) \\ 0, \ else \end{cases} \tag{8}$$

(x) A matrix $\boldsymbol{O}_1$ was first initialised to match the homogenised $\boldsymbol{O}$ matrix. Subsequently, for $k = 1 \ldots n_{r+1}$, each $\boldsymbol{O}_k$ matrix was recursively convolved n_r times using the square kernel $\boldsymbol{K}$ defined in Eq. (9), with $\boldsymbol{O}_k$ being redefined at each iteration according to Eq. (10). The iteration count n_r was determined via a for loop by applying the threshold condition specified in Eq. (11). Finally, the row and column indices of the pixels in $\boldsymbol{O}_{k+nr}$ that assumed the value 1 were taken to represent the optimal hole centre.

$$\boldsymbol{K} = \begin{pmatrix} 1 & 1 & 1 \\ 1 & 1 & 1 \\ 1 & 1 & 1 \end{pmatrix} \tag{9}$$

$$\boldsymbol{O}_{k+1} = \begin{cases} 1, \ o_{k,\ ij} = 9 \\ 0, \ else \end{cases} \tag{10}$$

$$\sum_{i=1}^{n} \sum_{j=1}^{m} o_{k,ij} \ \leq 1 \tag{11}$$

3. Materials and methods

Edge trimming and hole milling experiments were carried out on a 3 ± 0.3 mm-thick epoxy polymer-matrix composite plate reinforced with chopped (also known as forged), stochastically positioned and oriented carbon-fibre tows (ARRIS manufacture). The nominal fibre content of the composite was 67 wt%. The nominal tow length in the longitudinal direction was 13 mm. Fig. 4 presents the composite's surface appearance under varying illumination angles (M=10). Each panel depicts the identical region of interest, with light incident perpendicular to the longitudinal axis of the exposed carbon fibres.

A 100 × 140 mm specimen was edge trimmed under dry conditions with a feed rate (v_f) parallel to the 100 mm long edge, a depth of cut (a_p) equal to the plate thickness, and a width of cut (a_e) of 3 mm (Fig. 5a). Subsequently, 20 mm-diameter holes were milled in a 100 × 100 mm plate following the protocol shown in Fig. 5b–d. A pilot hole was first drilled, then enlarged to provide a uniform allowance for the hole milling experiments. A 10 mm-diameter, uncoated FRAISA solid-carbide tool (type 20360450) was employed. Cutting speed (v_c) and feed (f) were held constant at 160 m/min and 0.385 mm, respectively. Both down and up milling directions were investigated in the edge trimming experiments (Fig. 5a); then, based on the edge trimming outcomes, circular milling was performed exclusively under up milling conditions (Fig. 5d).

The machining experiments were conducted in the laboratory of the Department of Manufacturing Science and Engineering at Budapest University of Technology and Economics (Budapest, Hungary) using a three-axis Kondia B640 CNC milling machine. The machine's maximum spindle speed is 12 000 min^{-1}, driven by a 5.5 kW motor and controlled via an NCT301 unit. The working envelope measures 600 × 400 × 510 mm in the X (horizontal longitudinal), Y (horizontal transverse) and Z (vertical) axes, respectively. Nominal positioning accuracy is specified as ± 0.01 mm, repeatability as ± 0.005 mm, and the resolution of the relative measurement system as 0.001 mm. Chips generated within the machine enclosure were evacuated by a Nilfisk GB733 industrial vacuum cleaner, with a rated suction pressure of 14.7 kPa and volumetric flow of 73 l/s, so as to prevent abrasion of machine components by the carbon dust and to safeguard the health of the operating personnel.

3.1. Edge trimming

A Dino-Lite AM413ZT Pro digital microscope was fixed to the main spindle housing of the Kondia machining centre, and images of the composite plate were acquired at 20× nominal magnification and a resolution of 1280 × 1024 pixels both prior to and immediately following each machining experiment. Using this configuration, twenty images were recorded for each 100 mm length of machined edge (5 edges × 4 illumination directions), each image nominally depicting a 20

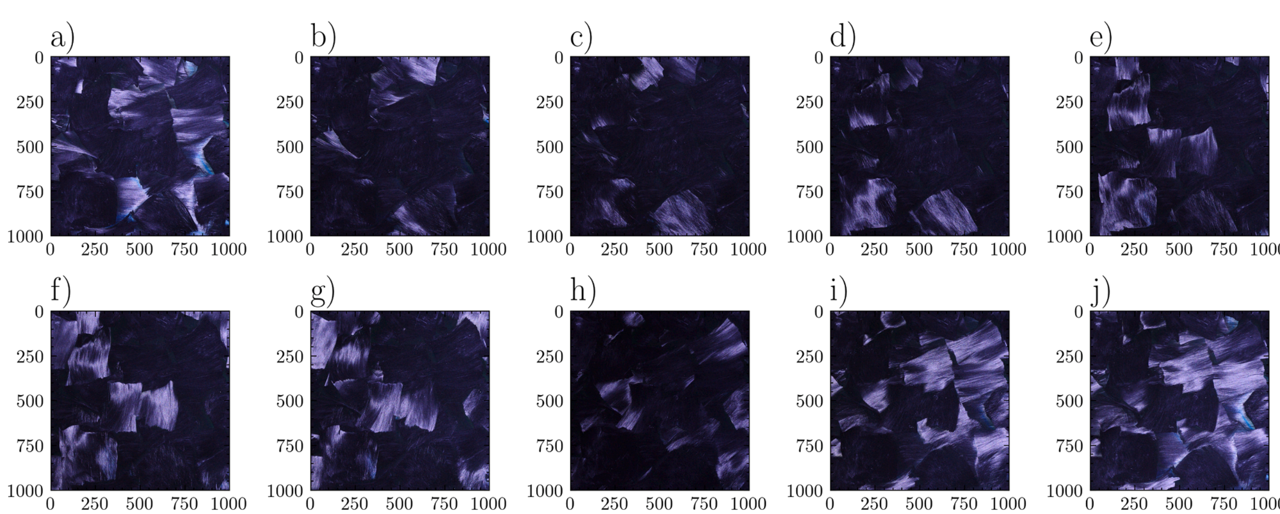

Fig. 4. Photographs (1000×1000 pixels) of the polymer-matrix composite plate reinforced with chopped, randomly oriented carbon-fibre tows, captured under varying illumination angles, where 1000 pixels is equal to 46.587 mm.

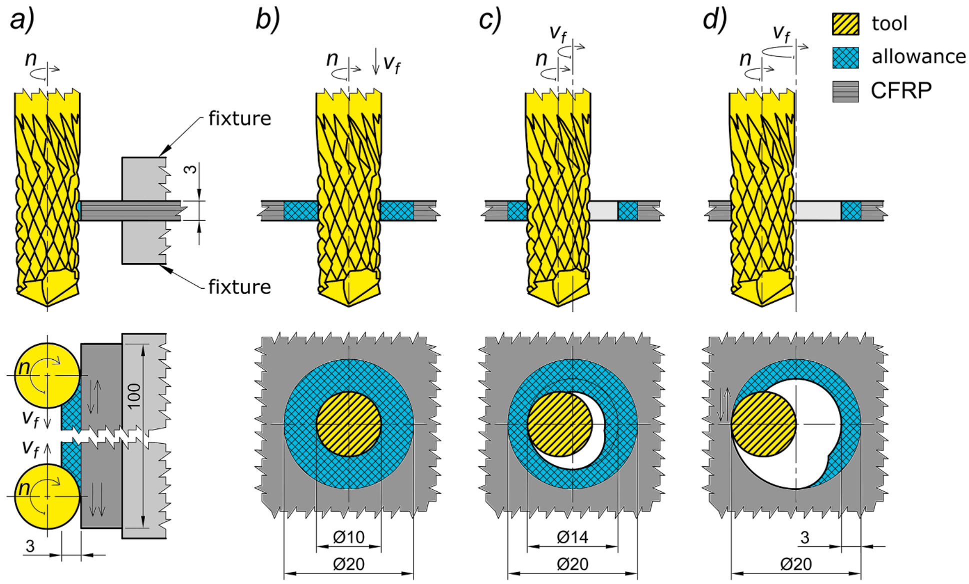

Fig. 5. A schematic illustration of the machining experiments in polymer composites reinforced by chopped carbon fibre tows: a) edge trimming using up and down milling technology, b) pilot hole drilling, c) hole-enlargement to provide uniform cutting width (a_e=3 mm) for the circular-milling experiments, d) circular-milling experiments using up-milling technology, where v_f denotes the feed rate and n is the spindle speed.

mm segment of edge. For every 20 mm segment, four images were captured under differing illumination azimuths—the lamp axis being nominally rotated about the machine's Y-axis by 0°, -45 °, -90 ° and -135 °—all at a fixed 45° incidence angle. Illumination was provided by a 3 W focusable LED source.

Image evaluation was conducted in AutoCAD according to the following procedure: **(i)** the captured images were imported into AutoCAD at a 1:1 scale with zero rotation; **(ii)** using the "Line" command (start- and end-point inputs), visibly distinct fibre tows, fibre orientations, burrs and delaminated regions were manually traced; **(iii)** features attributable to regenerative effects (e.g., delamination generated in a prior pass extending into the current cut width) were excluded from analysis; **(iv)** the fibre cutting angle (θ) along the machined contour was determined using the "Angle" measurement tool (two-line input); **(v)** burr length (L_b) and delamination depth (L_d) were measured as illustrated in Fig. 6 via the "Aligned" measurement tool (first point, then dynamic object-snap second point, producing a line perpendicular to the processed edge); **(vi)** within each fibre-cutting-angle bin, the maximum values of L_b and L_d were selected and tabulated for statistical analysis.

3.2. *Circular milling of holes*

The 100 × 100 mm CFRP plate was captured as described in [37], with each pixel corresponding to 0.117 mm. Two through holes of radius (r) of 10 mm were then machined via up milling (Fig. 5d). One hole was positioned at the site predicted to minimise the probability of machining-induced geometrical defects, whilst the second was located at the point of maximal predicted defect probability. Hole locations were determined using the algorithm presented in Section 2, taking into account insights gained from the edge trimming evaluations. The optimisation algorithm was implemented in Python within Visual Studio Code.

Hole quality was assessed using data supplied by a Keyence VR-500 3D surface profiler, which was processed by a custom Python routine. The principal steps of the evaluation algorithm were as follows: **(i)** the *.csv point-cloud data were imported into Visual Studio Code and represented as matrix $\boldsymbol{\alpha}$ (Eq. (12)), where $n = 1215$ and $m = 1023$, and NaN (not a number) entries denoting missing values; **(ii)** NaN entries in the $\boldsymbol{\alpha}$ matrix were filled by numerical interpolation; **(iii)** the $\boldsymbol{\alpha}$ matrix was segmented using a static threshold $\xi = -0.19$ (this value ensures that the hole, i.e., 2D circular disk area, is separated from the top surface located at cc. 0 mm) in accordance with Eq. (13);

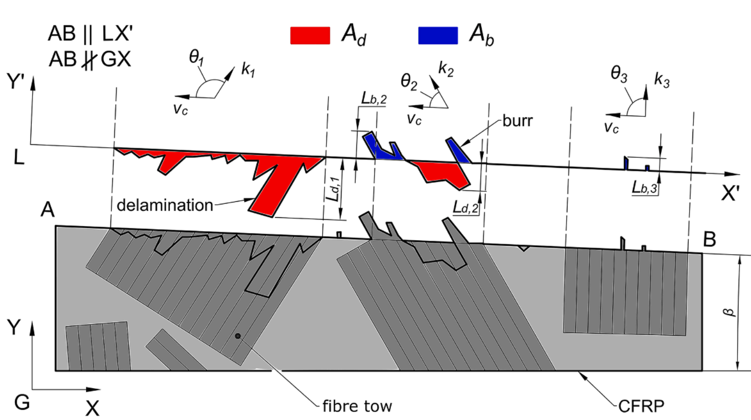

θ	L_b	L_d
θ_1	0	$L_{d,1}$
θ_2	$L_{b,2}$	$L_{d,2}$
θ_3	$L_{b,3}$	0

Fig. 6. A schematic illustration of the interpretation of the burr length (L_b) and delamination depth (L_d) at various fibre cutting angles (θ), where k denotes fibre direction.

$$\boldsymbol{\alpha} = \begin{pmatrix} \alpha_{11} & \cdots & \alpha_{1m} \\ \vdots & \ddots & \vdots \\ \alpha_{n1} & \cdots & \alpha_{nm} \end{pmatrix}, \ i = 1...n; j = 1...m, \ \alpha_{ij} \in \{-\infty ... + \infty; NaN\} \tag{12}$$

$$\boldsymbol{\beta} = \begin{pmatrix} \beta_{11} & \cdots & \beta_{1m} \\ \vdots & \ddots & \vdots \\ \beta_{n1} & \cdots & \beta_{nm} \end{pmatrix} = \begin{cases} 0, & \alpha_{ij} > \xi \\ 1, & else \end{cases},$$

$$i = 1...n; j = 1...m, \ \beta_{ij} \in \{0; 1\} \tag{13}$$

(iv) Matrix $\boldsymbol{\beta}_1$ was initialised to be identical to matrix $\boldsymbol{\beta}$. Subsequently, for k = 1 … $n_r + 1$, each $\boldsymbol{\beta}_k$ matrix was recursively convolved n_r times with the square kernel $\boldsymbol{K}$ defined in Eq. (14), $\boldsymbol{\beta}_k$ being redefined at each iteration in accordance with Eq. (15). The iteration count n_r was determined via a 'for' loop by applying the threshold criterion specified in Eq. (16);

$$\boldsymbol{K} = \begin{pmatrix} 1 & 1 & 1 \\ 1 & 1 & 1 \\ 1 & 1 & 1 \end{pmatrix} \tag{14}$$

$$\beta_{k+1} = \begin{cases} 1, & \beta_{k,\ ij} = 9 \\ 0, & else \end{cases} \tag{15}$$

$$\sum_{i=1}^{n} \sum_{j=1}^{m} \beta_{k,ij} \leq 1 \tag{16}$$

(v) the row and column indices of all elements in the $\boldsymbol{\beta}_{nr+1}$ matrix that assumed the value 1 were compiled into list L_1 using a brute force search; **(vi)** the n^{th} coordinate pair in L_1 (with $n = 1$ in this study) was then selected and interpreted as the pixel coordinates (i_y; j_x) of the hole centre; **(vii)** a matrix $\boldsymbol{C}$, of identical dimensions to $\boldsymbol{\beta}$, was generated to contain a segmented contour of thickness (th) of 3 pixels and radius of $(1 + 0.05)R$, centred at (i_y; j_x), where R denotes the hole radius expressed in pixels; **(viii)** by performing elementwise multiplication of $\boldsymbol{\beta}$ with $\boldsymbol{C}$, the $\boldsymbol{\gamma}$ matrix was obtained (per Eq. (17)), and its entries corresponding to the annular region were collected into list L_γ; **(ix)** the minimum and maximum values within L_γ were then determined, and the average contour height (H_a) and contour depth (H_z) indicators —introduced as analogues to ISO 21920-2:2021's Ra and Rz surface roughness metrics— were computed in accordance with Eq. (18) and Eq. (19).

$$\boldsymbol{\gamma} = \boldsymbol{C} \cdot \boldsymbol{\beta} \tag{17}$$

$$H_a = \frac{1}{n} \sum_{i=1}^{n} |L_{\gamma_i}| \tag{18}$$

$$H_z = \frac{1}{5} \sum_{j=1}^{m=5} \left(\max(L_{\gamma_i}) + |\min(L_{\gamma_i})| \right)_j, \ where:$$

$$i \in \begin{cases} \left\{0 ... \frac{n}{5}\right\}, & j = 1 \\ \left\{\frac{n}{5} ... \frac{2n}{5}\right\}, & j = 2 \\ \left\{\frac{2n}{5} ... \frac{3n}{5}\right\}, & j = 3 \\ \left\{\frac{3n}{5} ... \frac{4n}{5}\right\}, & j = 4 \\ \left\{\frac{4n}{5} ... n\right\}, & j = 5 \end{cases} \tag{19}$$

4×-magnification digital images of the holes were also obtained using an Olympus SZX16 stereo microscope. The segments of the hole contours exhibiting visible machining-induced burrs and delamination were manually delineated on these images. The pixel counts of the annotated arc segments were determined via a Python routine and subsequently normalised by the total pixel count of the hole contour in accordance with Eq. (20) and Eq. (21).

$$C_b = \frac{\sum_{j=1}^{m} c_{bj}}{\sum_{i=i}^{n} c_{0i}} \cdot 100 \tag{20}$$

$$C_d = \frac{\sum_{j=1}^{m} c_{dj}}{\sum_{i=i}^{n} c_{0i}} \cdot 100 \tag{21}$$

Where C_b denotes the specific burr-affected contour length, c_b is the number of burr-affected contour pixels, and c_0 is the nominal hole-contour pixel count; similarly, C_d denotes the specific delaminated contour length and c_d is the number of delaminated contour pixels. The interpretation of the C_b and C_d metrics is illustrated in Fig. 7.

4. Results and discussion

First, the results of edge trimming experiments (Fig. 5a) are presented and discussed in Section 4.1, to determine the parameters θ_c, δ_1 and δ_2 required for the optimisation procedure set out in steps i.–x. of Section 2. Then, Section 4.2 summarises and discusses the results of the circular milling experiments (Fig. 5d), aiming to validate the effectiveness of the proposed optimisation algorithm.

4.1. Edge trimming results

Representative digital images are shown in Fig. 8, in which the delaminated and burr-affected edge segments are readily apparent to the naked eye. Analysis of these images revealed that **(i)** the overall quality of edges machined by down milling —evaluated in terms of burr and delamination severity— is substantially poorer than that of edges produced by up milling, **(ii)** the occurrence of machining-induced burrs and delamination is governed primarily by the fibre-cutting angle, but is also significantly influenced by the milling strategy (up versus down) and by the longitudinal tow length. It was further observed that fibre tows oriented at critical angles exhibit only peel-up to the tow boundary, and that the maximum burr length never exceeds the axial distance between the tow's end and the machined edge contour. Although the insights relating to tow-axis length suggest promising avenues for future technological development, they fall outside the scope of the present study.

The observations made during visual inspection of the digital images are corroborated by the plots presented in Fig. 9 and Fig. 10. It is evident from these graphs that: **(i)** the burr measured on contours produced by up milling are typically an order of magnitude smaller than those observed following down milling; **(ii)** in the case of up milling, the range of fibre-cutting angles over which the probability of machining-induced burr and delamination formation is significant is markedly narrower; **(iii)** down milling yielded delamination depths nearly twice those recorded under up milling. During up milling, the theoretical chip thickness is zero at tool-workpiece engagement and then increases continuously with feed to the maximum value corresponding to the tool radius-wide cut. The sudden change in damping conditions at the moment of maximum engagement can induce torsional and bending vibrations in the tool, which may substantially influence, among other factors, the surface roughness of the machined part [39–42]. However, surface roughness is of secondary importance in the machining of CFRP composites, since their primary applications lie in lightweight, high-strength load-bearing structures where burr- and delamination-free assemblies are the chief optimisation criteria and micro-geometric accuracy is subordinate [43,44]. Although down milling is generally the preferred and recommended method for the majority of industrial materials [41], it is inadvisable to realise the maximum theoretical chip thickness at tool-entry in certain ceramics and CFRP composites – under the assumption of a constant specific cutting force,

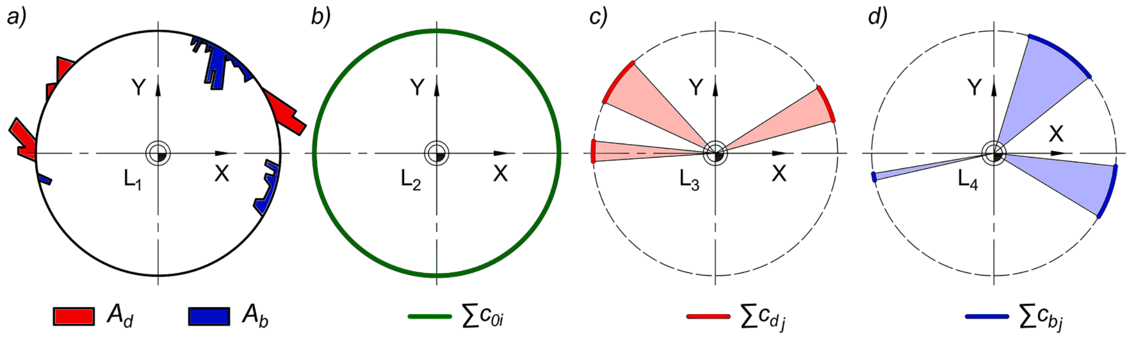

Fig. 7. A schematic illustration of the a) burr area (A_b) and delamination area (A_d), b) nominal hole contour, c) delamination contour and d) burr contour.

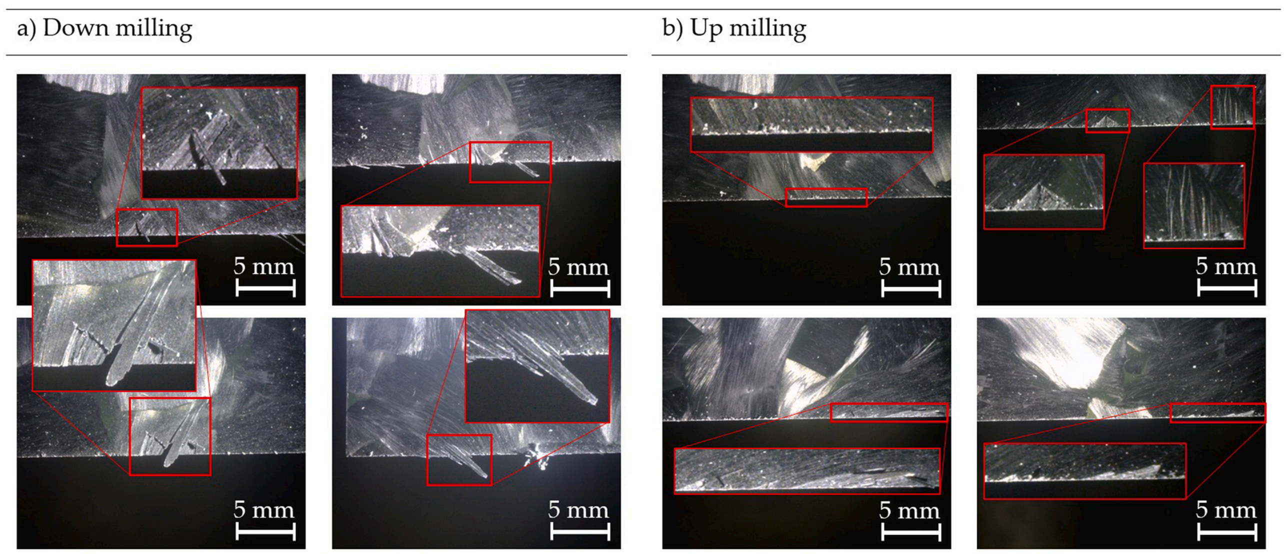

Fig. 8. Representative digital images of the CFRP composite surface produced by a) down milling and b) up milling.

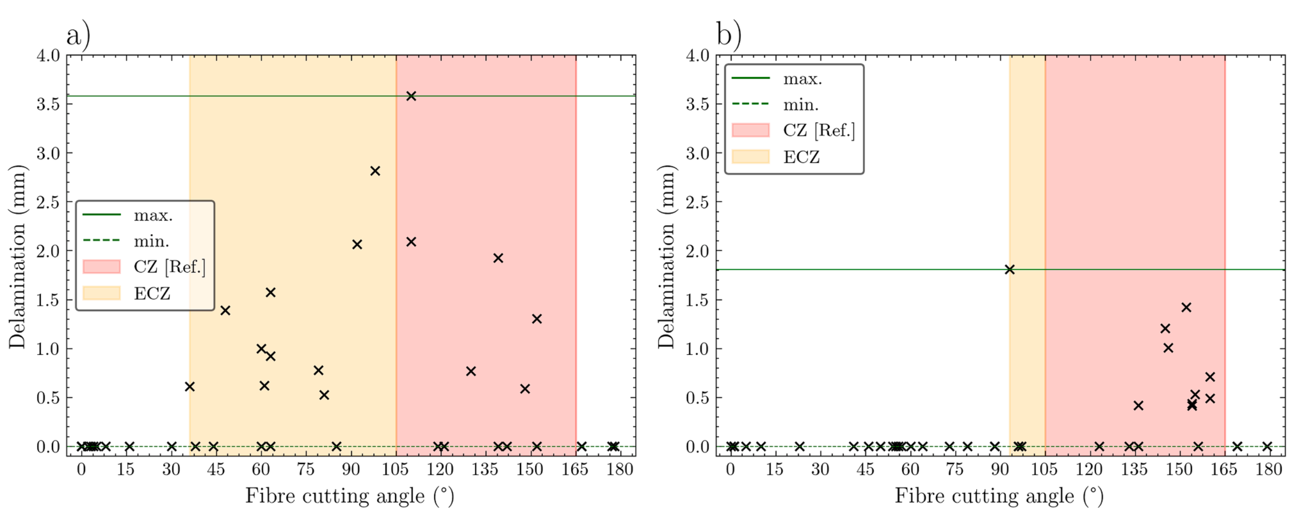

Fig. 9. Effect of the fibre cutting angle (θ) on the delamination depth (L_d) generated during a) down milling and b) up milling, where CZ denotes the critical zone of fibre cutting angle [37] and ECZ denotes the extended critical zone beyond CZ.

this results in the highest cutting forces and force variations.

Considering that the fibre cutting angle levels (as an independent variable) could not be controlled, owing to the stochastic distribution of fibre tows within the CFRP composite, the measured fibre cutting angles (81 data points) were categorised into twelve groups (θ_g) as listed in Table 1. This grouping effectively created multiple pseudo-replicates, thereby permitting analysis of variance (ANOVA) on the collected data.

Table 2 summarises the significance analysis, at a significance level (α) of 0.05, of the effects of the fibre cutting angle groups on the L_b and L_d indicators. The ANOVA results confirm that: **(i)** in down milling, the

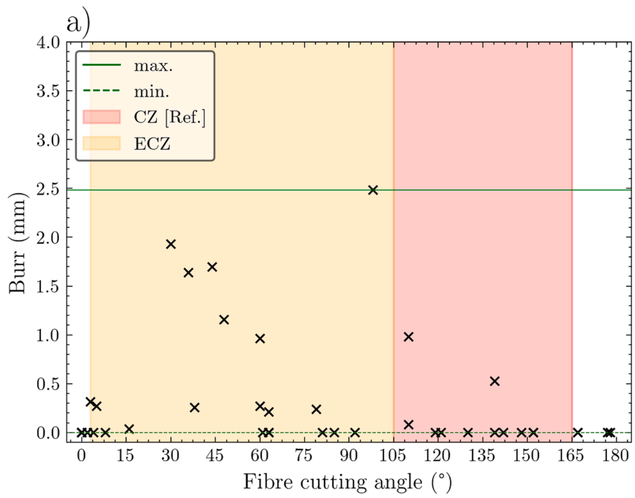

Fig. 10. Effect of the fibre cutting angle (θ) on the burr length (L_b) generated during a) down milling and b) up milling, where CZ denotes the critical zone of fibre cutting angle [37] and ECZ denotes the extended critical zone beyond CZ.

Table 1
Sorting measured fibre cutting angles (θ) into fibre cutting angle groups (θ_g).

θ (°)	(0; 15]	(15; 30]	(30; 45]	(45; 60]	(60; 75]	(75; 90]
θ_g (°)	7.5	22.5	37.5	52.5	67.5	82.5
θ (°)	(90; 105]	(105; 120]	(120; 135]	(135; 150]	(150; 165]	(165; 180]
θ_g (°)	97.5	112.5	127.5	142.5	157.5	172.5

Table 2
Analysis of variance (ANOVA) table, where P-values less than the α=0.05 significance level are bolded.

a) Down milling						
	Factor	DF	Adj SS	Adj MS	F-value	P-value
F_d:	θ_g	11	18.05	1.6406	3.57	**0.003**
F_b:	θ_g	11	8.627	0.7843	3.39	**0.004**
b) Up milling						
	Factor	DF	Adj SS	Adj MS	F-value	P-value
F_d:	θ_g	10	3.098	0.3098	2.07	0.060
F_b:	θ_g	10	0.034	0.0034	1.70	0.131

magnitude of machining-induced burrs and delamination depends significantly on the fibre-cutting angle. Consequently, knowledge of the fibre cutting angle allows for accurate prediction of defect formation; **(ii)** in up milling, the influence of fibre cutting angle on the L_b and L_d indicators is not significant; i.e., the fibre cutting angle alone is insufficient to estimate the severity of burrs or delamination. On this basis, down milling appears to be the more controllable and predictable strategy when considering the full (0°; 180°] range of fibre cutting angles. However, the proposed optimisation algorithm restricts the fibre cutting angle domain to approximately 0°–90°, within which all measured L_b and L_d values are zero under up milling. In other words, independent of the fibre cutting angle within this reduced range, the probability of machining-induced defects is minimised.

Considering that up milling yielded significantly superior edge contours, its application is recommended for the edge trimming of CFRP composites. It is further advised to restrict the fibre cutting angle along the machined contour to the 0°–90° range during process planning, as within this interval the likelihood of machining-induced burr and delamination formation is minimised. Based on the results of the up milling experiments and supporting literature, the critical fibre cutting angle (θ_c) is set to 135°, with the associated parameters δ_1 and δ_2 both defined as 44°.

4.2. Circular-milling results

Employing $\theta_c = 135°$, $\delta_1 = \delta_2 = 44°$, and a hole radius of $r = 10$ mm, the hole-position optimisation algorithm was executed to determine the optimal centre for the hole. The resulting $\boldsymbol{O}$ matrix (the sum of the convolved matrices as illustrated in Fig. 4**i**) is depicted in Fig. 11a. Lower values of the elements o_{ij} correspond to a reduced probability of significant machining-induced defects along the perimeter of a hole centred at that position. The spatial distribution of the o_{ij} elements is shown in Fig. 11b, and the homogenised $\boldsymbol{O}$ matrix is illustrated in Fig. 12a.

It is evident from the plots that the data span is considerable (1 910 pixels), indicating that hole position is likely to exert a significant influence on the hole quality. Following execution of the recursive convolution ($n_r = 13$), the element o_{ij} marked with a yellow "×" in Fig. 12b identified the optimal hole location. A hole was then circular-milled at this position by up milling (Fig. 5d) and designated as the "best-case."

The optimisation algorithm was subsequently re-run, this time with the objective function modified to select the centre corresponding to the poorest predicted quality (i.e., Eq. (22) was employed instead of Eq. (8)). The resulting hole centre is indicated by a red "×" in Fig. 12b and was labelled the "worst-case." A systematic comparison of the "best-case" versus "worst-case" holes validated the efficacy of the developed optimisation procedure.

$$o_{ij} = \begin{cases} 1, \ o_{ij} > (MAX - (\vartheta \cdot \mathrm{MAX})) \\ \quad 0, \ else \end{cases} \tag{22}$$

Fig. 13 presents the 3D point-cloud data of the best- and worst-case holes, as acquired by the 3D profilometer. In Fig. 13a, the homogeneity of the region adjacent to the best-case hole's contour is evident—indicating generally good quality—apart from a delaminated zone in the upper-left corner (see Fig. 14a). However, in the contour-adjacent region of the worst-case hole shown in Fig. 13b, substantial deviations from the reference plane (the zero-plane fitted to the upper surface of the CFRP plate) are observed at multiple locations (see

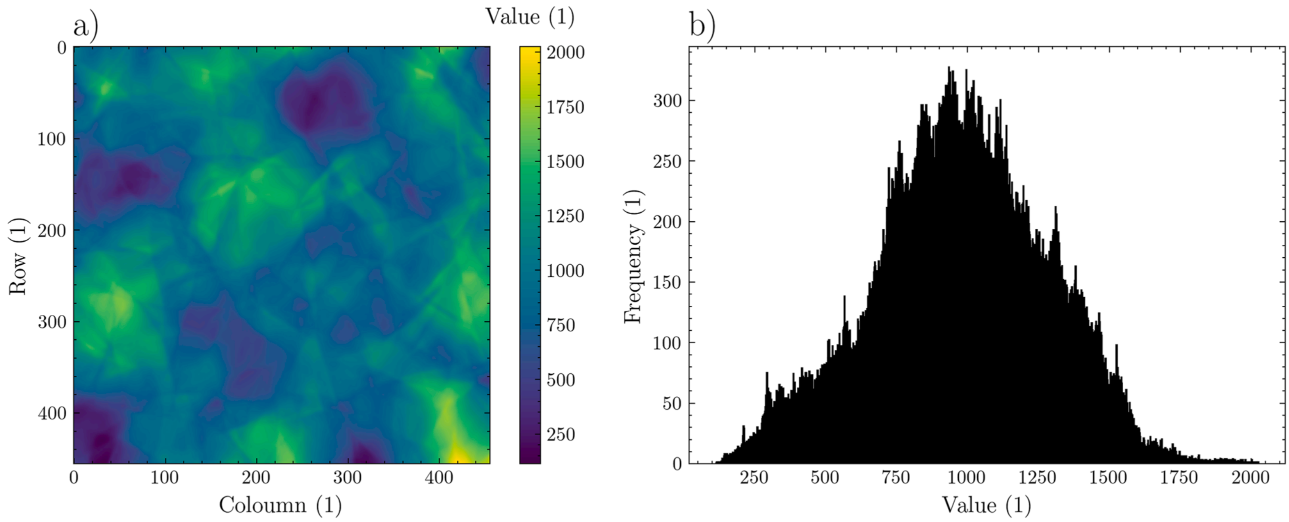

Fig. 11. Illustration of the a) $\boldsymbol{O}$ matrix and the b) spatial distribution of o_{ij} elements.

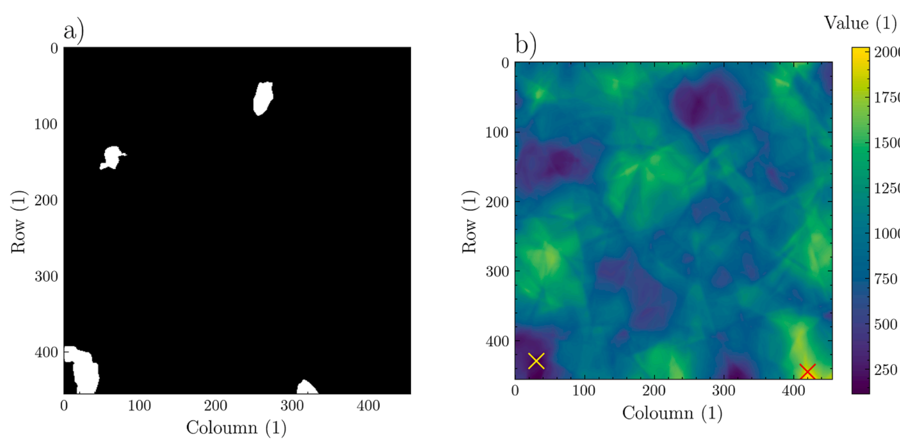

Fig. 12. a) Homogenised $\boldsymbol{O}$ matrix ($\vartheta = 0.1$) for determining the optimal hole centre; b) positions of the optimisation points (yellow "×" denotes the best-case, red "×" denotes the worst-case).

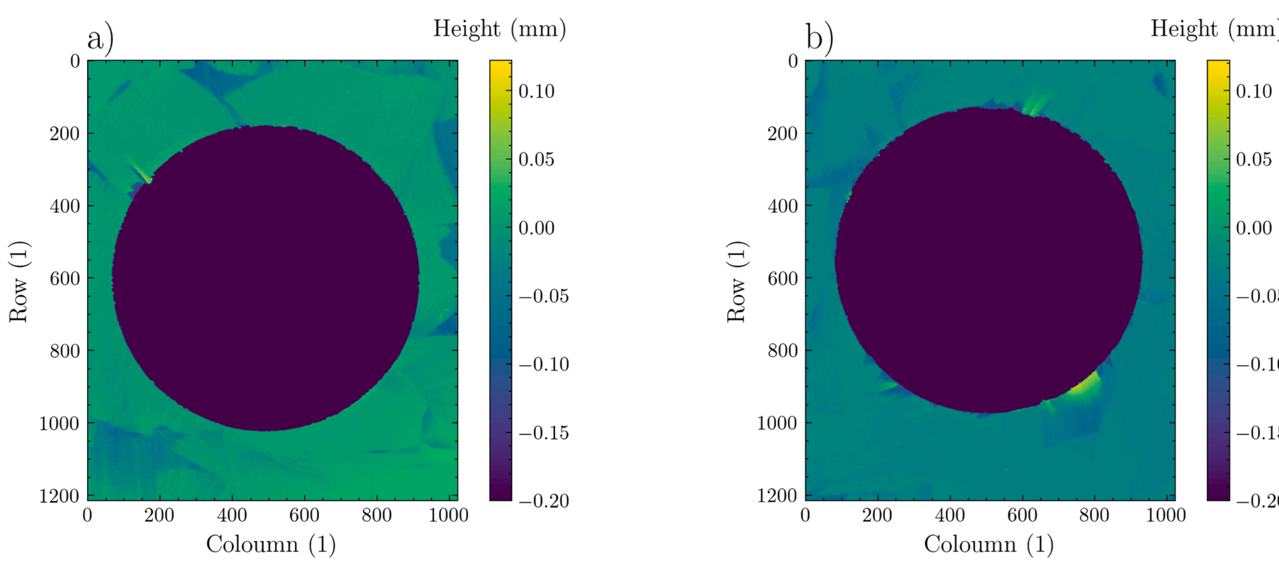

Fig. 13. 3D point-cloud data of the a) best- and b) worst-case holes.

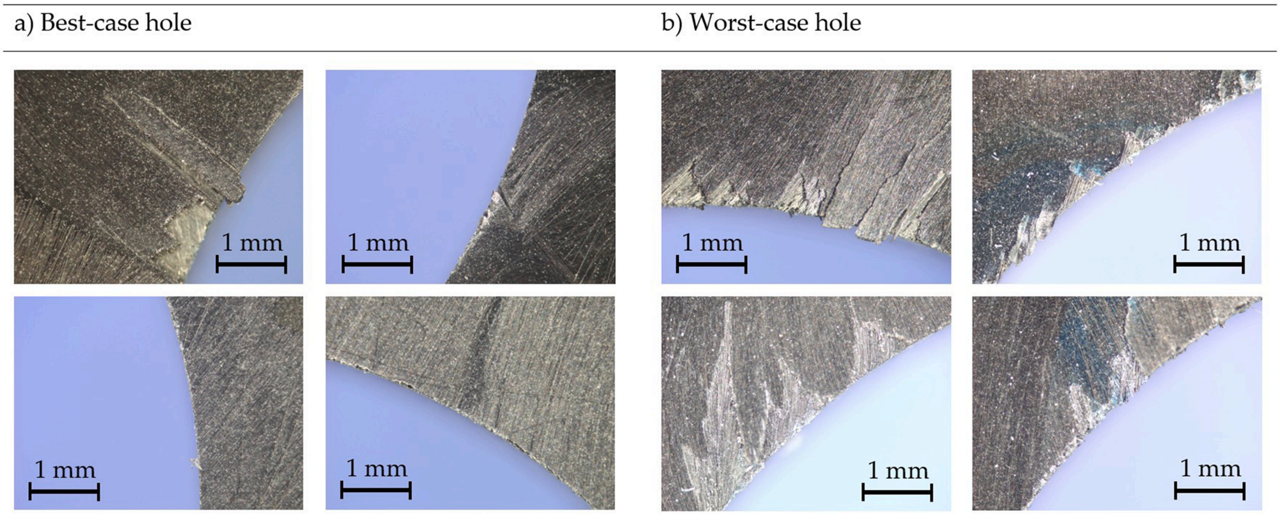

Fig. 14. Representative microscopic images of (a) the best-case hole and (b) the worst-case hole.

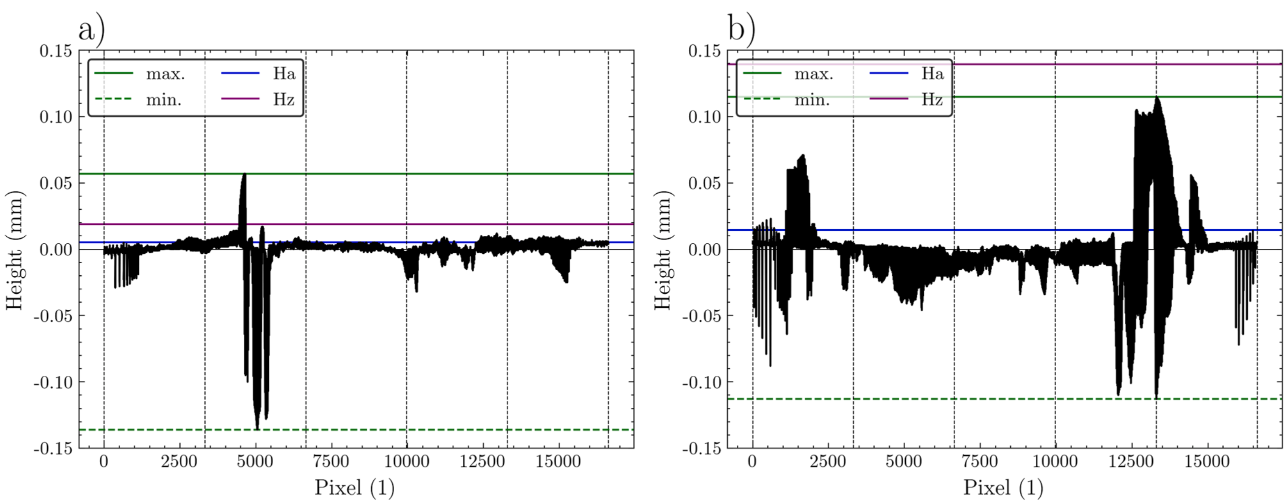

Fig. 15. Height of the data points around the a) best-case and b) worst-case holes, where H_a denotes the average contour height and H_z is the contour height, as expressed by Eq. (18) and Eq. (19), respectively.

Fig. 14b). Fig. 15 illustrates the data points extracted from an annular region concentric with the nominal hole contour, defined by radii $r_1 =$ 440 pixels and $r_2 =$ 443 pixels (the nominal hole radius is 433 pixels).

The superior quality of the best-case hole is illustrated in Fig. 15a, whereas that of the worst-case hole is shown in Fig. 15b. Analysis of the data revealed that: **(i)** the maximum deviation from the reference plane for the best-case hole was 50.44 % lower than that of the worst-case hole; **(ii)** the average contour height indicator H_a for the best-case hole was 64.99 % better than that of the worst-case hole; **(iii)** the contour depth indicator H_z for the best-case hole was 86.51 % better than that of the worst-case hole. Table 3 summarises the C_d and C_b indicators for the contour-adjacent segments of the holes. The C_d indicator for the best-case hole was 77.07 % higher than that of the worst-case hole, while the difference in the C_b indicator was 84.90 %. The comparative assessment of both the quantitative quality indicators and the qualitative micrographs confirms the relevance and efficiency of the developed hole-position optimisation algorithm.

Table 3
Summary of quality indicators of the best-case and worst-case holes.

Hole	*min*	*max*	H_a (mm)	H_z (mm)	C_d (1)	C_b (1)
best-case	-0.136	0.057	0.005	0.018	5.52 %	2.39 %
worst-case	-0.113	0.115	0.014	0.139	24.07 %	15.83 %

4.3. Discussion and outlook

Owing to limited resources, only the best- and worst-case scenarios could be experimentally validated. However, a numerical simulation assessed the maximum specific quality improvement attainable for 5, 10, 15, 20, 25 and 30 mm-diameter holes, considering the available machining allowance (called "distance" on the figure) on the investigated 100 × 100 mm composite plate. The results of the numerical simulation are presented in Fig. 16. The plot clearly shows that shifting the 20 mm diameter hole centre by 3 mm in the appropriate direction can yield a maximum quality enhancement of 49 %, while offsets of 6 mm and 9 mm correspond to maximal improvements of 63 % and 71 %, respectively. It can also be seen that the smaller the hole diameter to be machined, the larger the room for improvement. The reason for this is that the larger holes have longer edges, making it more difficult to avoid the critical fibre cutting angle range. In addition, the larger the hole diameter, the larger the probability of getting in contact with more fibre tows having different orientations. While Fig. 16 represent the

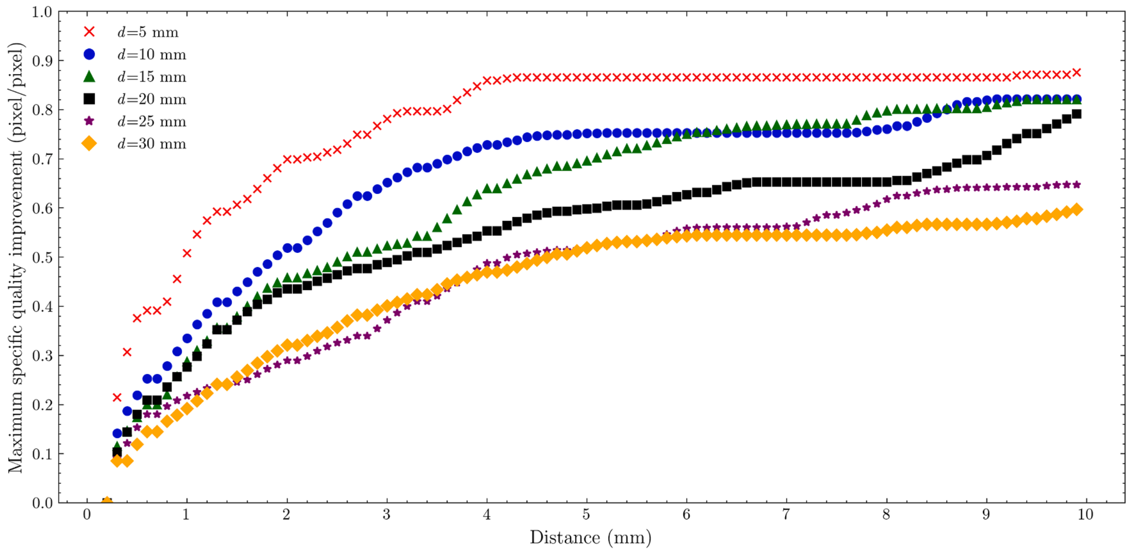

Fig. 16. Expected value of the maximum specific quality improvement in the function of the shift distance, considering hole diameters of 5, 10, 15, 20, 25 and 30 mm.

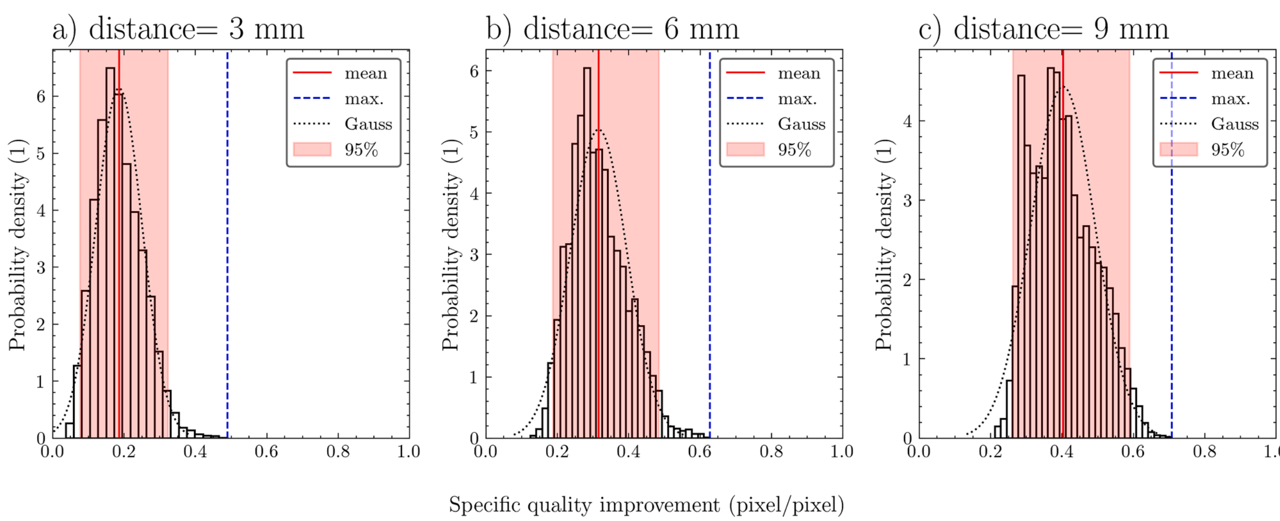

Fig. 17. Probability density graphs for a 20 mm diameter hole, if a) 3 mm, b) 6 mm and c) 9 mm are available for shifting the hole centre.

achievable improvements within the given distances, Fig. 17 lists all of the specific quality improvements available when the distance is 3, 6 or 9 mm if a 20 mm diameter hole is considered. The expected values (means of 18.6 %, 31.6 %, and 40,3 %, respectively) suggest that a slight room (3-9 mm) of improvement results in significant quality improvement, while at least 20 % improvement is achievable if the allowance is 9 mm thick (Fig. 17c).

In industrial settings, the likelihood of choosing the absolute worst hole location within a given area is low. To better illustrate the advantages of the proposed method relative to current best practices (rather than relative to the worst-case scenarios), an additional numerical analysis was conducted. Fig. 18 contrasts the minimal specific defect attainable using the proposed algorithm with that obtained by positioning the hole at the area's geometric centre (the nominal approach). The data reveal that opportunities for improvement grow as the nominal specific defect and the maximum allowable shift distance increases. Specifically, when the nominal specific defect is above 60 %, the proposed approach yields an average quality gain of 12 % if the allowable shift distance is 3 mm (Fig. 18a). For larger shift distances, this average improvement rises to 22 % (Fig. 18b) and 30 % (Fig. 18c), respectively.

Based on the experimental and numerical results, it is recommended that the allowance-planning process for composite plates be augmented to include analysis of the expected quality and potential quality improvements of machined geometric features by exploiting the proposed fibre-orientation-driven defect probability mapping.

The optimisation algorithm, currently validated at Technology Readiness Level 4 (laboratory scale), exhibits the following scope conditions and limitations, which should be targeted when considering industrial implementation: **(i)** The carbon-fibre tows are embedded in a polymer matrix that must remain optically clear. Any tinting or opacifying additives (e.g., UV stabilisers, flame retardants) could reduce contrast in the image-processing stage, leading to misidentification of fibre boundaries. For instance, a semi-opaque gel-coat layer commonly used on marine CFRP panels would require adjustment of illumination intensity or a switch to near-infrared imaging. **(ii)** The method assumes tow axes are nominally horizontal (within $\pm5°$). In highly curved or woven laminates, where tows change orientation through the thickness, additional calibration or 3D imaging (e.g., computer tomography) may be required to maintain angle-detection accuracy. **(iii)** To maximise brightness differences, the approach requires minimal transverse

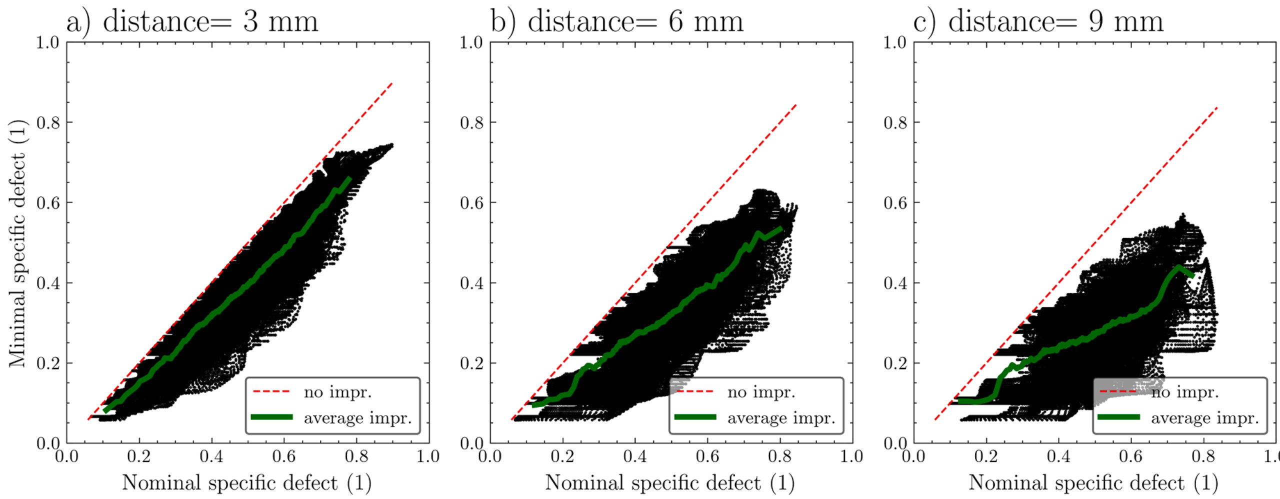

Fig. 18. Scatterplots of the specific defect of 20 mm diameter holes machined into a state-of-the-art position (i.e., middle of the given area) vs. best possible position by exploiting fibre orientation, if a) 3 mm, b) 6 mm and c) 9 mm are available for shifting the hole centre.

grooving on the fibre surfaces. The more severe the transverse grooving on the fibres is, the less the difference in the brightness of a parallel and perpendicular tow relative to the light direction, making the segmentation process even more difficult. **(iv)** A well-impregnated matrix with strong fibre–matrix adhesion is essential to prevent pre–existing interlaminar delamination from confounding burr detection. Vacuum-assisted resin transfer moulding composites with known dry-spot risks may introduce spurious "false positives" unless resin infusion protocols are optimised. **(v)** At present, the algorithm marks contour points simply as "burr present" or "burr absent." Future refinements could implement multi-level scoring (e.g., small, medium, large burr) by exploiting information on the remaining embedded fibre tow length. **(vi)** It is assumed that burrs do not coalesce around the perimeter; each defect is localised. In practice, burr merging can occur on small diameter holes or intricate pocket contours, necessitating cluster-analysis techniques to separate contiguous burr regions. **(vii)** The current implementation uses images ≈0.12 mm/pixel. Higher-resolution imaging (e.g., 4 K cameras) can improve defect sensitivity down to sub-0.05 mm features but will increase computational load and demand more robust noise-reduction strategies. **(viii)** The optimiser currently explores only translations (x, y) of a circular feature within the preform allowance. For non-circular or anisotropic geometries, such as elongated slots or rib-reinforced panels, a 3D search (x, y, α) and corresponding 3D $\boldsymbol{O}$-tensor will be required to capture all viable positioning permutations. **(ix)** Presently, each pixel is classified as defective (1) or not (0). In future, a probabilistic model —leveraging, for example, Gaussian processes— could provide a continuous defect likelihood, enabling risk-based decision thresholds (e.g., 90 % confidence contours). **(x)** Although the proposed algorithm is validated through circular-milling experiments, its effectiveness for drilling technology has to be investigated in the future along with analysing the influence of the peel-up and push-down effects of drilling on the critical fibre cutting angle range. **(xi)** The current 2D image processing of the surface of the composite can determine fibre cutting angle along the nominal hole contour at the composite surface; thus, machining-induced geometrical effects, which form mainly at the machined edges (such as delamination and burr), can be effectively controlled. However, effects along the depth of the composite (such as fibre pull-outs, matrix smearing, interlayer burrs and delamination, etc.) cannot be controlled by using the proposed method; only 3D imaging (e.g., computer tomography) would provide enough data for mapping the fibre tow directions inside the composite. **(xii)** The hyperparameters of the algorithm were optimised in this study to maximise the extraction of relevant information from 2D images. However, these hyperparameters may require re-tuning when applied to different conditions, such as variations in composite material properties, lighting setups, or camera specifications.

By articulating these constraints and potential extensions, practitioners can judge the applicability of the algorithm to their specific manufacturing scenarios and identify the necessary adaptations —such as imaging hardware upgrades, algorithm retraining, or expanded search domains— to achieve reliable burr and delamination minimisation in CFRP composite machining.

5. Conclusions

An innovative optimisation algorithm has been developed to improve the quality of circular-milled holes in polymer composites reinforced by chopped carbon fibre tows by exploiting local fibre orientation. Key findings and contributions are as follows:

- A multi-stage digital image processing and convolution approach was formulated, producing a response matrix ($\boldsymbol{O}$) whose minima correspond to the hole position with minimal machining-induced geometrical defect (burr and delamination) risk. Experimental validation on a 20 mm-diameter hole demonstrated that the "best-case" position reduced average contour height (H_a) by 64.99 % and contour depth (H_z) by 86.51 % compared with the "worst-case" position. Burr- and delamination-area metrics (C_b, C_d) were similarly improved by 84.90 % and 77.07 %, respectively.
- Up milling was confirmed to yield markedly superior edge quality compared with down milling, exhibiting burr heights an order of magnitude lower and a significantly narrower critical fibre cutting angle range for defect formation.
- A critical fibre cutting angle ($\theta_c = 135^\circ \pm 44^\circ$) was identified, and limiting the fibre cutting angle domain within 0°–90° under up milling eliminated measurable defects.
- Numerical simulations indicate that modest translational shifts of 3, 6 or 9 mm from the nominal hole centre can deliver theoretical quality gains of 49 %, 63 % and 71 %, respectively, underscoring the value of allowance-planning integration in composite part design and manufacturing technology planning.
- The method is readily implementable on standard three-axis CNC mills and relies on off-the-shelf imaging hardware and open-source Python routines, facilitating adoption in industrial settings.
- At present, the algorithm assumes binary defect detection, pure translational searches for circular features, and homogenous, transparent polymer matrices with minimal tow deformation and low fibre volume fraction. Future developments should extend the search

space to include rotations and non-circular feature geometries, adopt continuous probabilistic defect models, and investigate applicability to less-transparent or high-fibre-content composites. High-resolution imaging and advanced machine-learning segmentation are also envisioned to enhance sensitivity to sub-0.05 mm defects.

In conclusion, the proposed hole-position optimisation framework achieves significant defect mitigation in CFRP machining and offers a practical pathway for integrating burr- and delamination-minimisation strategies into composite-part design and manufacturing process planning. Ongoing work will focus on expanding the method's generality, refining its probabilistic modelling, and validating performance across diverse composite architectures and machining technologies.

Declarations

Funding: Not applicable

Availability of data and material: The data that support the findings of this study are available from the corresponding author, upon reasonable request.

Code availability: Not applicable.

Ethics approval: Not applicable.

Consent to participate: Not applicable.

Consent for publication: Not applicable.

Declaration of generative AI and AI-assisted technologies in the writing process: During the preparation of this work, the author used ChatGPT in order to improve the English text. After using this tool, the author reviewed and edited the content as needed and takes full responsibility for the content of the publication.

CRediT authorship contribution statement

Norbert Geier: Writing – review & editing, Writing – original draft, Visualization, Validation, Supervision, Software, Resources, Project administration, Methodology, Investigation, Funding acquisition, Formal analysis, Data curation, Conceptualization.

Declaration of competing interest

The author declare that he has no known competing financial interests or personal relationships that could have appeared to influence the work reported in this paper.

Acknowledgements

This research was supported by the János Bolyai Research Scholarship of the Hungarian Academy of Sciences No. BO/00508/22/6. The author acknowledges the technical support of Dániel István Poór, Levente Bukor, György Póka and Gergely Magyar in the preparation works and discussions.

Data availability

Data will be made available on request.

References

[1] Y. Chen, Y. Ji, X. Hu, Residual flexural properties of surface scratched CFRP laminates with diverse span lengths and thickness profiles, J. Mater. Res. Technol. 36 (2025) 4453–4463, https://doi.org/10.1016/j.jmrt.2025.04.124.
[2] N. Geier, J. Paulo Davim, T. Szalay, Advanced cutting tools and technologies for drilling carbon fibre reinforced polymer (CFRP) composites: a review, Compos. Part A: Appl. Sci. Manuf. 125 (2019) 105552, https://doi.org/10.1016/j.compositesa.2019.105552.
[3] N. Geier, J. Xu, D.I. Poór, J.H. Dege, JP. Davim, A review on advanced cutting tools and technologies for edge trimming of carbon fibre reinforced polymer (CFRP) composites, Compos. Part B: Eng. 266 (2023) 111037, https://doi.org/10.1016/j.compositesb.2023.111037.
[4] F. Su, L. Zheng, F. Sun, Z. Wang, Z. Deng, X. Qiu, Novel drill bit based on the step-control scheme for reducing the CFRP delamination, J. Mater. Process. Technol. 262 (2018) 157–167, https://doi.org/10.1016/j.jmatprotec.2018.06.037.
[5] F. Wang, M. Zhao, R. Fu, X. Liu, S. Qiu, J. Yan, et al., Replaceable drill bit with compound step and sawtooth structures for damages and drilling-cost reduction of CFRP composite, J. Manuf. Process. 81 (2022) 1018–1027, https://doi.org/10.1016/j.jmapro.2022.07.001.
[6] Z. Jia, R. Fu, B. Niu, B. Qian, Y. Bai, F. Wang, Novel drill structure for damage reduction in drilling CFRP composites, Int. J. Machine Tools Manuf. 110 (2016) 55–65, https://doi.org/10.1016/j.ijmachtools.2016.08.006.
[7] Z. Jia, C. Zhang, F. Wang, R. Fu, C. Chen, Multi-margin drill structure for improving hole quality and dimensional consistency in drilling Ti/CFRP stacks, J. Mater. Process. Technol. 276 (2020) 116405, https://doi.org/10.1016/j.jmatprotec.2019.116405.
[8] N. Geier, T. Szalay, Optimisation of process parameters for the orbital and conventional drilling of uni-directional carbon fibre-reinforced polymers (UD-CFRP), Measurement 110 (2017) 319–334, https://doi.org/10.1016/j.measurement.2017.07.007.
[9] L. Sorrentino, S. Turchetta, C. Bellini, A new method to reduce delaminations during drilling of FRP laminates by feed rate control, Compos. Struct. 186 (2018) 154–164, https://doi.org/10.1016/j.compstruct.2017.12.005.
[10] N. Khanna, F. Pusavec, C. Agrawal, GM. Krolczyk, Measurement and evaluation of hole attributes for drilling CFRP composites using an indigenously developed cryogenic machining facility, Measurement 154 (2020) 107504, https://doi.org/10.1016/j.measurement.2020.107504.
[11] S. Amini, M. Baraheni, E. Hakimi, Enhancing dimensional accuracy and surface integrity by helical milling of carbon fiber reinforced polymers, Int. J. Lightweight Materials Manuf. (2019), https://doi.org/10.1016/j.ijlmm.2019.03.001.
[12] C. Pereszlai, N. Geier, D.I. Poór, B.Z. Balázs, G. Póka, Drilling fibre reinforced polymer composites (CFRP and GFRP): An analysis of the cutting force of the tilted helical milling process, Compos. Struct. 262 (2021) 113646, https://doi.org/10.1016/j.compstruct.2021.113646.
[13] V. Schulze, W. Spomer, C. Becke, A voxel-based kinematic simulation model for force analyses of complex milling operations such as wobble milling, Prod. Eng. Res. Devel. 6 (2012) 1–9, https://doi.org/10.1007/s11740-011-0348-4.
[14] Y. Lu, S. Yuan, Y. Chen, A cutting force model based on kinematic analysis in longitudinal and torsional ultrasonic vibration drilling, Int. J. Adv. Manuf. Technol. 104 (2019) 631–643, https://doi.org/10.1007/s00170-019-03884-y.
[15] W. Huang, S. Cao, H.N. Li, Q. Zhou, C. Wu, D. Zhu, et al., Tool wear in ultrasonic vibration–assisted drilling of CFRP: a comparison with conventional drilling, Int. J. Adv. Manuf. Technol. 115 (2021) 1809–1820, https://doi.org/10.1007/s00170-021-07198-w.
[16] Z. Feng, F. Jiao, Study on exit damage characteristics of ultrasonic vibration assisted drilling of CFRP, Adv. Mech. Eng. 14 (2022) 16878132221100653, https://doi.org/10.1177/16878132221100653.
[17] Z. Sun, D. Geng, F. Meng, L. Zhou, X. Jiang, D. Zhang, High performance drilling of T800 CFRP composites by combining ultrasonic vibration and optimized drill structure, Ultrasonics. 134 (2023) 107097, https://doi.org/10.1016/j.ultras.2023.107097.
[18] C. Wang, K. Cheng, R. Rakowski, D. Greenwood, J. Wale, Comparative studies on the effect of pilot drillings with application to high-speed drilling of carbon fibre reinforced plastic (CFRP) composites, Int. J. Adv. Manuf. Technol. 89 (2017) 3243–3255, https://doi.org/10.1007/s00170-016-9268-y.
[19] G-D Wang, MS. Kirwa, Comparisons of the use of twist, pilot-hole and step-drill on influence of carbon fiber-reinforced polymer drilling hole quality, J. Compos. Mater. 52 (2018) 1465–1480, https://doi.org/10.1177/0021998317726366.
[20] A. Dogrusadik, A. Kentli, Experimental investigation of support plates' influences on tool wear in micro-drilling of CFRP laminates, J. Manuf. Process. 38 (2019) 214–222, https://doi.org/10.1016/j.jmapro.2019.01.018.
[21] A. Dogrusadik, A. Kentli, Effect of support plates on the micro-drilled hole form quality in CFRP laminates, Materials Testing 61 (2019) 467–476, https://doi.org/10.3139/120.111343.
[22] X. Kong, Z. Dang, X. Liu, M. Wang, A comparative evaluation of laser assisted drilling CFRP with improved machining mechanism, J. Mater. Process. Technol. 321 (2023) 118156, https://doi.org/10.1016/j.jmatprotec.2023.118156.
[23] X. Kong, Y. Wang, X. Liu, Z. Dang, M. Wang, Research on the removal mechanism and surface damage of laser assisted cutting of CFRP materials, J. Manuf. Process. 124 (2024) 196–211, https://doi.org/10.1016/j.jmapro.2024.06.006.
[24] J. Ahmad, Machining of Polymer Composites, Springer US, 2009.
[25] J. Deng, F. Wang, R. Fu, Y. Lin, Q. He, X. Ma, Prediction of time-varying dynamics and chatter stability analysis for surface milling of thin-walled curved CFRP workpiece, J. Mater. Process. Technol. 322 (2023) 118186, https://doi.org/10.1016/j.jmatprotec.2023.118186.
[26] A. Abena, S.L. Soo, K. Essa, Modelling the orthogonal cutting of UD-CFRP composites: Development of a novel cohesive zone model, Compos. Struct. 168 (2017) 65–83, https://doi.org/10.1016/j.compstruct.2017.02.030.
[27] L. Chen, K. Zhang, H. Cheng, Z. Qi, Q. Meng, A cutting force predicting model in orthogonal machining of unidirectional CFRP for entire range of fiber orientation, Int. J. Adv. Manuf. Technol. 89 (2017) 833–846, https://doi.org/10.1007/s00170-016-9059-5.
[28] N. Geier, Influence of fibre orientation on cutting force in up and down milling of UD-CFRP composites, Int. J. Adv. Manuf. Technol. 111 (2020) 881–893, https://doi.org/10.1007/s00170-020-06163-3.
[29] W. Hintze, G. Shchegel, J. Mehnen, C. Möller, J. Dege, Model based assessment of maximal surface temperatures and heat flow in edge trimming of UD CFRP with

tools of different type, Compos. Part B: Eng. 300 (2025) 112483, https://doi.org/10.1016/j.compositesb.2025.112483.

[30] A. Brouschkin, L. Köttner, W. Hintze, J. Dege, Prediction of Surface Profile in CFRP Machining through Phenomenological Analysis and inverse Continuous Wavelet Transformation, Procedia CIRP. 123 (2024) 143–148, https://doi.org/10.1016/j.procir.2024.05.027.

[31] X. Wang, G. Bi, Q. Zhang, F. Wang, R. Fu, Improvement of geometry of multi-tooth milling cutter for surface damage suppression in milling of CFRP with theoretical method, J. Manuf. Process. 142 (2025) 84–98, https://doi.org/10.1016/j.jmapro.2025.03.093.

[32] D. István Poór, N. Geier, C. Pereszlai, J. Xu, A critical review of the drilling of CFRP composites: Burr formation, characterisation and challenges, Compos. Part B: Eng. (2021) 109155, https://doi.org/10.1016/j.compositesb.2021.109155.

[33] C. Wang, L. Wen, W. Ming, Q. An, M. Chen, Experimental study on effects of fiber cutting angle in milling of high-strength unidirectional carbon fiber–reinforced polymer laminates, Proceed. Instit. Mechan. Eng., Part B: J. Eng. Manuf. 232 (2018) 1813–1824, https://doi.org/10.1177/0954405416679868.

[34] F. Wang, P. Chen, R. Fu, G. Bi, Effects of cutting speed and fiber orientation on tool wear and machining quality in milling CFRP with PCD cutter, Proceed. Institut. Mechan. Eng., Part B: J. Eng. Manuf. 237 (2023) 1364–1375, https://doi.org/10.1177/09544054221130396.

[35] M. Qian, J. Xiao, G. Wang, P. Huang, Z. Chen, G. Han, Evaluation of heat generation using a microscopic cutting model with thermo-mechanical coupling for carbon fiber reinforced polymer composites, J. Reinf. Plast. Compos. 39 (2020) 793–804, https://doi.org/10.1177/0731684420931589.

[36] N. Geier, G. Magyar, J. Giner, T. Lukács, G. Póka, Carbon fibre detection in polymer composites reinforced by chopped carbon fibres through digital image processing and machine learning, J. Compos. Mater. 58 (2024) 2379–2395, https://doi.org/10.1177/00219983241268861.

[37] N. Geier, G. Póka, Á Jacsó, C. Pereszlai, A method to predict drilling-induced burr occurrence in chopped carbon fibre reinforced polymer (CFRP) composites based on digital image processing, Compos. Part B: Eng. 242 (2022) 110054, https://doi.org/10.1016/j.compositesb.2022.110054.

[38] N. Geier, G. Magyar, Advanced allowance planning of CFRP composites exploiting the pattern of chopped carbon fibre reinforcement clusters, Procedia CIRP. 131 (2025) 130–135, https://doi.org/10.1016/j.procir.2024.09.021.

[39] W. Xu, Q. Li, L. Wang, Q. Feng, S. Yuan, Analysis of the effect of different milling strategies on the surface quality of multiphase fibers and particle reinforced polymer matrix composites, Compos. Part A: Appl. Sci. Manuf. 193 (2025) 108847, https://doi.org/10.1016/j.compositesa.2025.108847.

[40] P. Michalik, J. Zajac, M. Hatala, D. Mital, V. Fecova, Monitoring surface roughness of thin-walled components from steel C45 machining down and up milling, Measurement 58 (2014) 416–428, https://doi.org/10.1016/j.measurement.2014.09.008.

[41] T. Insperger, B.P. Mann, G. Stépán, PV. Bayly, Stability of up-milling and down-milling, part 1: alternative analytical methods, Int. J. Machine Tools Manuf. 43 (2003) 25–34, https://doi.org/10.1016/S0890-6955(02)00159-1.

[42] B.P. Mann, T. Insperger, P.V. Bayly, G. Stépán, Stability of up-milling and down-milling, part 2: experimental verification, Int. J. Machine Tools Manuf. 43 (2003) 35–40, https://doi.org/10.1016/S0890-6955(02)00160-8.

[43] D. Geng, Y. Liu, Z. Shao, Z. Lu, J. Cai, X. Li, et al., Delamination formation, evaluation and suppression during drilling of composite laminates: A review, Compos. Struct. 216 (2019) 168–186, https://doi.org/10.1016/j.compstruct.2019.02.099.

[44] N. Geier, C. Pereszlai, Analysis of characteristics of surface roughness of machined CFRP composites, Periodica Polytechnica 64 (2020) 67–80, https://doi.org/10.3311/PPme.14436.